

Assessing astrophysical foreground subtraction in DECIGO using compact binary populations inferred from the first part of the LIGO-Virgo-KAGRA's fourth observation run

Takahiro S. Yamamoto  ^{1,*}

¹*Research Center for the Early Universe (RESCEU),
Graduate School of Science, The University of Tokyo, Tokyo 113-0033, Japan*

(Dated: January 27, 2026)

Detecting the stochastic gravitational wave background (SGWB) from our Universe under the inflationary era is one of the primary scientific objectives of DECIGO, a space-borne gravitational wave detector sensitive in the ~ 0.1 Hz frequency band. This frequency band is dominated by the gravitational waves from inspiraling compact object binaries. Subtracting these signals is necessary to search for the primordial SGWB. In this paper, we assess the feasibility of the subtraction of such binary signals by employing the population model inferred from the latest gravitational wave event catalogue of the LIGO-Virgo-KAGRA Collaboration. We find that the projection scheme, which was originally proposed by Cutler & Harms (2005), is necessary to reduce the binary signals to the level where DECIGO can detect the primordial background.

I. INTRODUCTION

It is believed that our Universe experienced the accelerated expansion, called *inflation*, at its very beginning. Although there are many mechanisms to realize the inflationary expansion, no concrete conclusion has been achieved yet. One of the keys to unveiling the inflationary universe is the primordial stochastic gravitational wave background (SGWB) that originates from the quantum fluctuation of the tensor perturbation. In this work, we consider the space-based laser interferometer DECIGO [1] as a probe of the primordial SGWB. DECIGO has the sensitivity at the frequency band from 0.01 Hz to 10 Hz, and their configurations can be optimized for searching primordial SGWB (see Sec. II A).

One of the difficulties for DECIGO to detect the primordial SGWB is the presence of a lot of compact binaries, such as binary neutron stars (BNSs) and binary black holes (BBHs). Gravitational waves (GWs) they emit overlap each other and form the astrophysical SGWB whose power is $O(10^{4-5})$ times larger than the primordial one. Several strategies have been proposed to address this issue so far. Biscoveanu *et al.* [2] proposes the Bayesian approach to search for the primordial SGWB in the presence of the astrophysical foreground. Their algorithm simultaneously estimates the parameters characterizing the primordial SGWB and those characterizing the BBH foreground. The global fit [3, 4] offers another approach in the context of LISA [5], the space-borne interferometers aiming for GWs in 1 mHz frequency band. It is expected to observe a lot of signals overlapping each other in the time domain. The global fit estimates the source parameters for all binaries simultaneously and efficiently, which can be utilized to remove the foreground and search for the primordial SGWB [6].

Cutler & Harms [7] takes the approach to subtract the best-fit waveform of each binary signal. Many of compact binary coalescences (CBCs) can be identified as individual binaries if they have enough amplitudes for DECIGO to detect. Once we detect them, we can estimate their source parameters and reconstruct their waveform. By subtracting the reconstructed waveforms from the strain data, we can remove the astrophysical SGWB. The remaining components originate from parameter estimation errors and from binaries not detected as individual events. Zhu *et al.* [8] takes this approach to assess the foreground with the ground-based detectors.

In this paper, we assess how effectively the subtraction scheme could suppress the astrophysical SGWB, assuming the latest LIGO-Virgo-KAGRA (LVK) Collaboration catalog and inferred population. We follow Cutler & Harms [7] and Rosado [9] for the estimation of the astrophysical SGWB. The population model is taken from the LVK Collaboration's latest catalog and the inferred population and mass distributions. In Sec II, we explain the settings for our calculation, such as the signal and detector noise model, the population of BBHs and BNSs, and the procedure for calculating the foreground. As we explain in section II C, the astrophysical foreground can be decomposed into three components. We calculate each of them to explicitly show how these three components behave, while assessing the subtractable components is enough to discuss the feasibility of the foreground subtraction. After presenting the results in Sec III, we conclude the paper in Sec IV. Appendix A explains the subtraction strategy and its details for estimating the foreground. The script we used in this work is available from https://github.com/tsyamamoto21/subtraction_estimate.

* yamamoto.s.takahiro@resceu.s.u-tokyo.ac.jp

II. METHOD

A. Signal model and detector setup

DECIGO is a space-based laser interferometer that was originally proposed by Seto *et al.* [10]. The configuration is shown in Figure. 1. Its basic unit consists of three satellites that are located at the corners of an equilateral triangle with the side length of 1000 km. The unit orbits around the Sun with maintaining its triangular formation. Each satellite has two free-falling mirrors that serve as test masses. Each pair of two satellites forms a Fabry-Perot cavity and measures the changes in arm lengths induced by gravitational waves. A triangle-shaped laser interferometer is equivalent to two independent L-shaped interferometers that are located at the same place and have orientations with 45 degree offset. The ultimate configuration of DECIGO consists of four units. Two of them are located at different positions on the heliocentric orbit. The other two units are colocated and have the opposite direction, indicated by the six-pointed star in the Figure 1. The star-like configuration is useful for the correlation analysis. The SGWB, whose realization is determined by a random process, would be detected by taking the correlation between two or more independent detectors. This is a reason why the star-like configuration is proposed. From the star-like configuration, we can calculate the correlations between two L-shaped interferometers with their arms aligned. As a result, the star-like configuration provides us with two correlations. In the

following, we assume that we have eight independent L-shaped interferometers and two streams of correlations. We denote them by

$$N_{\text{det}} = 8, \quad N_{\text{corr}} = 2. \quad (2.1)$$

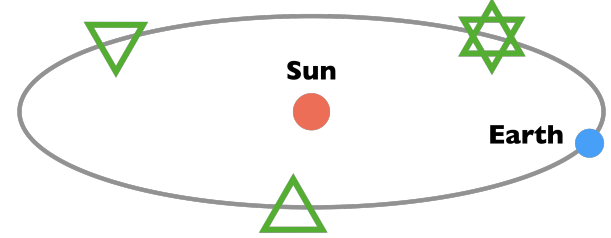


FIG. 1. Configuration of DECIGO. In this work, we assume two triangle-shaped constellations and one six-pointed star consteration.

The noise level of the laser interferometers is characterized by the power spectral density (PSD), denoted by $S_n(f)$. It is defined from the Fourier transform of the noise $\tilde{n}(f)$ by

$$\langle |\tilde{n}(f)\tilde{n}^*(f')| \rangle = \frac{1}{2}S_n(f)\delta(f-f'). \quad (2.2)$$

We use the PSD shown in [11],

$$S_n(f) = 7.05 \times 10^{-48} \cdot \left(1 + \left(\frac{f}{f_p}\right)^2\right) + 4.8 \times 10^{-51} \cdot \left(\frac{f}{1 \text{ Hz}}\right)^{-4} \cdot \frac{1}{1 + (f/f_p)^2} + 5.33 \times 10^{-52} \cdot \left(\frac{f}{1 \text{ Hz}}\right)^{-4} \text{ Hz}^{-1}, \quad (2.3)$$

with $f_p = 7.36 \text{ Hz}$. Figure 2 shows the PSD of DECIGO.

In this work, we only use the inspiral part of the binaries. We use the angle-averaged GW signal.

$$\tilde{h}(f; \mathcal{M}_c, z) = \frac{\sqrt{3}}{2} \mathcal{A}(\mathcal{M}_c, z) f^{-7/6} e^{i\Psi(f; \mathcal{M}_c)}, \quad (2.4)$$

where $\mathcal{A}(\mathcal{M}_c, z)$ is the amplitude, and $\Psi(f; \mathcal{M}_c)$ is the phase. The amplitude is defined by

$$\mathcal{A}(\mathcal{M}_c, z) = \frac{1}{\sqrt{30\pi^{2/3}}} \frac{((1+z)\mathcal{M}_c)^{5/6}}{d_L(z)}, \quad (2.5)$$

with the chirp mass $\mathcal{M}_c = (m_1 m_2)^{3/5} / (m_1 + m_2)^{1/5}$ and the luminosity distance $d_L(z)$. The explicit expression of $\Psi(f)$ is not given here since we only care about the signal-to-noise ratio (SNR) in which only the amplitude affects (see Eq. (2.6)). We use the cosmological parameters inferred by the observational results of Planck18 [12] via the library `astropy`. The SNR of the inspiral signal

with N_{det} detectors is computed in the frequency domain,

$$\rho(\mathcal{M}_c, z) = \sqrt{N_{\text{det}}} \cdot \left[4 \int_0^\infty df \frac{|\tilde{h}(f; \mathcal{M}_c, z)|^2}{S_n(f)} \right]^{1/2}. \quad (2.6)$$

Substituting Eqs. (2.4) and (2.5) to Eq. (2.6), we get

$$\rho(\mathcal{M}_c, z) = \frac{\sqrt{N_{\text{det}}}}{\sqrt{10\pi^{2/3}}} \cdot \frac{\mathcal{M}_c^{5/6}}{d_L(z)} \left[\int_0^\infty df \frac{f^{-7/3}}{S_n(f)} \right]^{1/2}, \quad (2.7)$$

with

$$\mathcal{M}_z = (1+z)\mathcal{M}_c. \quad (2.8)$$

B. Population model

We follow the reference [13] for calculating the merger rate density. The merger rate density of BBHs is modeled

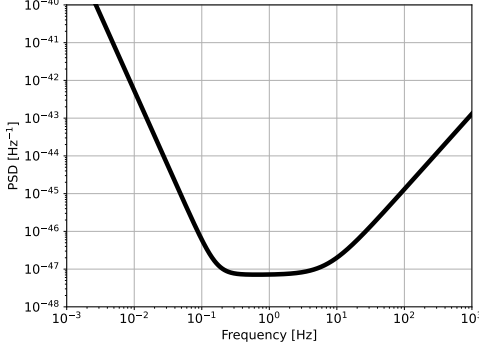


FIG. 2. PSD of DECIGO that is taken from Yagi & Seto [11]

by the double power-law,

$$R_{\text{BBH}}(z; \alpha, \beta, z_p) = C \frac{(1+z)^\alpha}{1 + \left(\frac{1+z}{1+z_p}\right)^{\alpha+\beta}}, \quad (2.9)$$

with $\alpha = 3.2$, $\beta = 5.1$, and $z_p = 2.6$. The constant C is chosen so that Eq. (2.9) satisfies

$$R_{\text{BBH}}(z=0) = 20 \text{ Gpc}^{-3} \text{ yr}^{-1}. \quad (2.10)$$

For BNSs, we assume that the BNS formation rate $\psi(z)$ follows the star formation rate and is modeled by the same functional form as Eq. (2.9) with $\alpha = 2.6$, $\beta = 3.6$, and $z_p = 2.2$. The merger rate density $R_{\text{BNS}}(z)$ is calculated by convoluting the star formation rate $\psi(z)$ and the delay time distribution, that is,

$$R_{\text{BNS}}(z) = A \int_{t_{\text{d}}^{\text{min}}}^{\infty} dt_{\text{d}} p(t_{\text{d}}) \frac{\psi(z_f)}{1+z_f} \quad (0 \leq z \leq 10), \quad (2.11)$$

and $R(z) = 0$ for $z > 10$. The time delay, t_{d} , is the interval between a binary formation and the binary merger. Its distribution $p(t_{\text{d}})$ is proportional to t_{d}^{-1} . The minimum delay is set at 50 Myr for BNS. The constant A is chosen so that the merger rate density at $z = 0$ satisfies

$$R_{\text{BNS}}(z=0) = 100 \text{ Gpc}^{-3} \text{ yr}^{-1}. \quad (2.12)$$

For the mass distribution, we used the population model inferred from GWTC-4 [14, 15]. We employ `SimpleUniform` for BNS, in which the component masses follow the uniform distribution on $[1.0, 2.5] M_{\odot}$. For BBH, we used the `BrokenPowerLaw+TwoPeaks` model. We obtain the posterior samples from Zenodo repository [16] and use the median values for the hyperparameters characterizing the mass spectrum. In this work, we assume that the mass distribution does not depend on the redshift.

C. SGWB

The strength of SGWB is characterized by the density parameter, Ω_{gw} , which is defined by the energy density

of the SGWB divided by the critical density. For the primordial SGWB, the simplest inflation model predicts the flat spectrum in DECIGO's frequency band. In this work, referring to the Planck18's result [12], we use

$$\Omega_{\text{gw}}(f) \equiv 10^{-16}, \quad (2.13)$$

as a fiducial value. We calculate the astrophysical SGWB generated by the ensemble of compact binaries by following the method used in Rosado [9] and Cutler & Harms [7]. The energy spectrum of GW from a binary is given by

$$\frac{dE_{\text{gw}}}{df_r} = \frac{\pi^{2/3}}{3} \frac{G^{2/3} \mathcal{M}_c^{5/3}}{f_r^{1/3}}, \quad (2.14)$$

where f_r is the frequency in the source's rest frame that relates to the frequency in the detector frame by $f_r = (1+z)f$. The energy spectrum of a binary in logarithmic scale is denoted by

$$P(f, z) = \left[f_r \frac{dE_{\text{gw}}}{df_r} \right]_{f_r=(1+z)f}. \quad (2.15)$$

The astrophysical foreground is calculated by integrating the energy spectrum of a binary over the relevant redshift range. We define the minimum and the maximum redshift, denoted by z_{min} and z_{max} respectively, that no binaries are assumed to exist outside of the redshift range from z_{min} and z_{max} . In this work, we fix them at

$$z_{\text{min}} = 0, \quad z_{\text{max}} = 10. \quad (2.16)$$

The integration range of the redshift should be determined with accounting for the merger frequencies and the GW frequencies shifting as the source distance. In this work, we use the frequency at the last stable orbit, which is defined by

$$f_{\text{max}} = \frac{1}{6\sqrt{6}\pi} \frac{c^3}{G(m_1 + m_2)}, \quad (2.17)$$

as a proxy for the merger frequency. The minimum frequency is the frequency at $T_{\text{obs}} = 3$ yr before the merger. It can be written as

$$f_{\text{min}} = \left[\frac{T_{\text{obs}}}{\delta_2} + f_{\text{max}}^{-8/3} \right]^{-3/8} \simeq \left[\frac{T_{\text{obs}}}{\delta_2} \right]^{-3/8}, \quad (2.18)$$

with

$$\delta_2 = \frac{5c^5}{256\pi^{8/3}(G\mathcal{M}_c)^{5/3}}. \quad (2.19)$$

We define the lower limit z_{low} and the upper limit z_{upp} to indicate the integration range of the redshift.

$$z_{\text{upp}}(f) = \begin{cases} z_{\text{max}} & f \leq \frac{f_{\text{max}}}{1+z_{\text{max}}}, \\ \frac{f_{\text{max}}}{f} - 1 & \frac{f_{\text{max}}}{1+z_{\text{max}}} < f < \frac{f_{\text{max}}}{1+z_{\text{min}}}, \\ z_{\text{min}} & \frac{f_{\text{max}}}{1+z_{\text{min}}} \leq f. \end{cases} \quad (2.20)$$

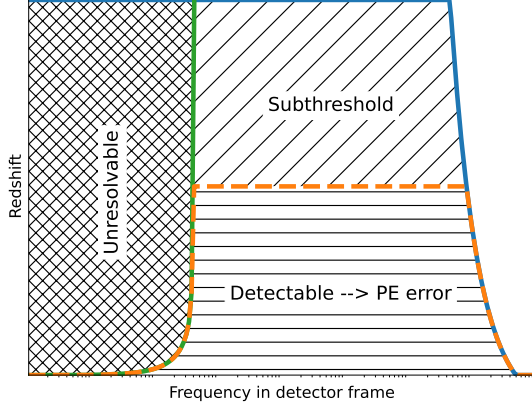


FIG. 3. Three components of the foreground. The cross-hatched region is the unresolvable part contributing to Ω_{unres} . Binaries in the region hatched by the diagonal lines generate the subthreshold component, Ω_{subth} . The region hatched by the horizontal lines corresponds to the detectable part, in which binaries can be detected as individual events. The errors in parameter estimation for these binaries contribute Ω_{err} . The blue line shows z_{upper} defined by Eq (2.20). The green line is z that is defined by Eq. (2.25). The orange dashed line is the upper bound of the detectable region. The right blank region indicates that there are no BNSs because it is a frequency band above the last stable orbit, and we ignore the merger and the post-merger part.

and

$$z_{\text{low}}(f) = \begin{cases} z_{\text{max}} & f \leq \frac{f_{\text{min}}}{1+z_{\text{max}}}, \\ \frac{f_{\text{min}}}{f} - 1 & \frac{f_{\text{min}}}{1+z_{\text{max}}} < f < \frac{f_{\text{min}}}{1+z_{\text{min}}}, \\ z_{\text{min}} & \frac{f_{\text{min}}}{1+z_{\text{min}}} \leq f. \end{cases} \quad (2.21)$$

They depend on the source parameters, particularly on the chirp mass. We do not indicate the dependency on the source parameter to make the notation simple. The density parameter $\Omega_{\text{fg}}(f)$ of the astrophysical foreground is calculated by

$$\Omega_{\text{fg}}(f) = \frac{1}{\rho_c c^2} \left\langle \int_{z_{\text{low}}}^{z_{\text{upp}}} dz \frac{R(z)P(f, z)}{H(z)(1+z)^2} \right\rangle_s, \quad (2.22)$$

where $\langle \cdot \rangle_s$ implies the average over the source parameters, $H(z)$ and ρ_c are the Hubble parameter and the critical density, respectively.

D. Foreground subtraction and its residual

In this subsection, we explain the strategy for subtracting the astrophysical foreground and our estimate of the

residuals that will remain in the strain data after subtraction. These residuals contribute a noise source in the sense that we cannot detect the primordial SGWB if the residual dominates.

We assume two strategies for subtracting the astrophysical foreground. In the first strategy, we search the signals from binaries, estimate their source parameters, and subtract the waveforms with the best-fit parameters from the strain data. The second strategy employs the projection scheme originally proposed by Cutler & Harms [7]. After subtracting the best-fit waveforms, as we did in the first strategy, the residuals will remain in the strain data. These residual has a component that is tangential to the waveform hypersurface in the high-dimensional signal space. By using the projection operator, defined by Eq. (A13), the tangential components can be suppressed, leading to further suppression of the subtraction errors.

The residual can be decomposed into three parts: the unresolvable part, the subthreshold part, and the parameter estimation (PE) error part. Figure 3 shows that the redshift and frequency plane is divided into the subregions corresponding to the above three components. The unresolvable part mostly appears in the low-frequency band. In general, the lower the orbital frequency of the binary, the slower the frequency evolution. The binary with the lower orbital frequency tends to stay in the same frequency bin for a long time. If two or more binaries coexist within one frequency bin during the entire observational period, you cannot resolve and separate them. This is the origin of the unresolvable part. The subthreshold part consists of binaries with SNR below the detection threshold. Binaries with SNR above the threshold can be detected as individual events and will be subtracted. The residuals from estimation errors accumulate to form the PE error component. In the following, we evaluate each residual component to clarify which components may potentially pose difficulties in the detection of the primordial SGWB.

First, we estimate the unresolvable part denoted by Ω_{unres} . To estimate the unresolvable part, we need the information about how many binaries are within a given frequency resolution at a given redshift. The number of binaries within the redshift z and located in the frequency range from f to $f + \Delta f$ is

$$\mathcal{N}(f, \Delta f, z) = \left\langle \int_{z_{\text{low}}}^z dz' \tau_e(f, \Delta f, z'; \theta) \dot{N}(z'; \theta) \right\rangle_s. \quad (2.23)$$

$\tau_e(f, \Delta f, z; \theta)$ is the time interval where a binary with the source parameter θ at the redshift of z spends from the frequency of f to $f + \Delta f$. It is calculated by

$$\tau_e(f, \Delta f, z; \theta) = \delta_2(1+z)^{-8/3} \left[f^{-8/3} - (f + \Delta f)^{-8/3} \right], \quad (2.24)$$

with δ_2 defined by Eq. (2.19). $\dot{N}(z; \theta)$ is the number of binaries with the source parameter θ at the redshift z . At a given frequency f and a frequency resolution Δf ,

we can calculate the redshift \mathfrak{z} below where one binary is expected to exist. By this definition, the redshift \mathfrak{z} is calculated by solving the equation

$$\mathcal{N}(f, \Delta f, \mathfrak{z}) = 1. \quad (2.25)$$

The unresolvable part can be calculated by

$$\Omega_{\text{unres}}(f) = \frac{1}{\rho_c c^2} \left\langle \int_{z_1}^{z_{\text{upp}}} dz' \frac{R(z') P(f, z)}{(1+z')^2 H(z')} \right\rangle_s, \quad (2.26)$$

with $z_1 := \min[\mathfrak{z}, z_{\text{low}}]$. Accounting for DECIGO's configuration more seriously, we may still resolve the binaries even when they are located within a single frequency bin. In this work, we naively set the criterion that binaries within one frequency bin can not be resolved.

Second, we estimate the PE error part. A binary detectable as an individual event satisfies the condition of

$$\rho(\mathcal{M}_c, z) \geq \rho_{\text{th}}, \quad (2.27)$$

with the detection threshold ρ_{th} . The redshift z_{th} is naturally defined by $\rho(\mathcal{M}_c, z_{\text{th}}) = \rho_{\text{th}}$. In this work, we use the following considerations to assess the contribution from the parameter estimation errors. The assumption that the waveform does not have systematics due to mismodeling is implicitly made. Various effects, such as eccentricity, spin-orbit precession, and environmental effects, can affect the GW signals and be the source of the systematics. They are out of the scope of this paper. Thus, we ignore them for the present paper. We approximate the contribution to Ω_{err} from each binary by

$$\frac{dE_{\text{gw}}}{d \ln f_r} \rightarrow \frac{dE_{\text{gw}}}{d \ln f_r} \times \frac{N_p}{\rho^2} \quad (2.28)$$

where N_p is the number of source parameters characterizing each binary. This estimation is described in Appendix A 1. We estimate Ω_{err} by

$$\Omega_{\text{err}}(f) = \frac{1}{\rho_c c^2} \left\langle \int_{z_{\text{low}}}^{z_2} dz \frac{R(z) P(f, z)}{H(z)(1+z)^2} \cdot \frac{N_p}{\rho^2} \right\rangle_s, \quad (2.29)$$

with $z_2 := \min[\mathfrak{z}, z_{\text{th}}, z_{\text{upp}}]$, which is indicated by the orange dashed line in Fig. 3.

Cutler & Harms proposed the scheme suppressing Ω_{err} by projecting out the first order of the parameter deviation from the residual. The scheme is outlined in the Appendix A 2. After the projection, the residual errors are dominated by the second order of the parameter estimation errors. Its power is evaluated by

$$\frac{dE_{\text{gw}}}{d \ln f_r} \times \frac{|\delta^P h|^2}{|h|^2} \sim \frac{dE_{\text{gw}}}{d \ln f_r} \times \left(\frac{N_p}{\rho^2} \right)^2. \quad (2.30)$$

Therefore, we estimate the foreground components generated from the subtraction residuals after the projection by

$$\Omega_{\text{err}}^P(f) = \frac{1}{\rho_c c^2} \left\langle \int_{z_{\text{low}}}^{z_2} dz \frac{R(z) P(f, z)}{H(z)(1+z)^2} \cdot \left(\frac{N_p}{\rho^2} \right)^2 \right\rangle_s. \quad (2.31)$$

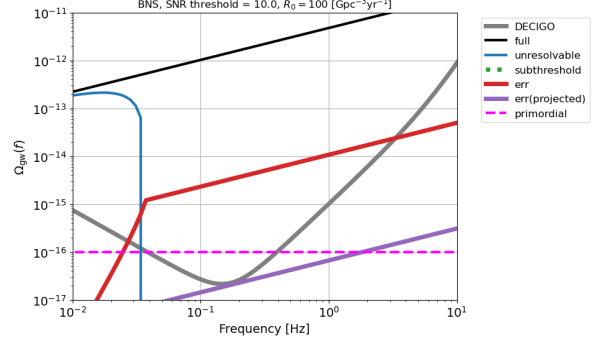


FIG. 4. Astrophysical foreground of BNSs and the subtracted residuals. We assume the SNR threshold of 10. The black thin line shows the total foreground. The blue thin line is the unresolvable component. The red thick and purple thick lines are the subtraction residual and the projected one, respectively. The green dotted line is the subthreshold component, which is too small to appear in this plot. The gray line is the minimum amplitude of $\Omega_{\text{gw}}(f)$ that can be detectable by DECIGO with the SNR larger than unity. The magenta dashed line shows the fiducial value 10^{-16} of the primordial GW background.

In the end, we estimate the subthreshold part. The subthreshold component Ω_{subth} consists of the binaries with the SNR less than the detection threshold. Using the definition of z_{th} , we estimate the subthreshold component by

$$\Omega_{\text{subth}}(f) = \frac{1}{\rho_c c^2} \left\langle \int_{z_2}^{z_3} dz \frac{R(z) P(f, z)}{H(z)(1+z)^2} \right\rangle_s, \quad (2.32)$$

with $z_3 := \min[\mathfrak{z}, z_{\text{upp}}]$.

We calculate the average over the source parameters by using Monte-Carlo sampling with the sample size of 1000.

III. RESULT

Figure 4 shows the estimations of the astrophysical foreground and the subtraction results for the case of BNSs with $R(z = 0) = 100 \text{ Gpc}^{-3} \text{ yr}^{-1}$ and $\rho_{\text{th}} = 10$. DECIGO's sensitivity for SGWB is also plotted by the gray solid line. The SNR threshold is small enough so that the subthreshold components are well below the primordial components and other foreground components. In the frequency band below 0.04 Hz, the unresolvable components dominate. Above that region, the subtraction error becomes the dominant one in the foreground. Without the projection, the foreground by the subtraction errors Ω_{err} is larger than the primordial components by from 1 to 2 orders of magnitude. This means we cannot detect the primordial components only by subtracting the best-fit waveforms. The projection scheme reduces it by about two orders of magnitude, making the subtraction errors below the primordial SGWB. This

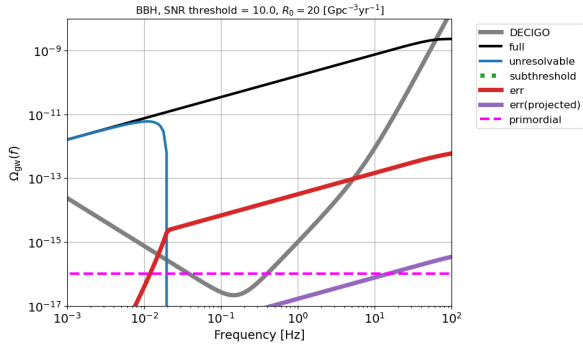


FIG. 5. Foreground estimation for BBH. The legends are the same as Fig. 4, while the plot ranges of the frequency and $\Omega_{\text{gw}}(f)$ are broader than those of Fig. 4.

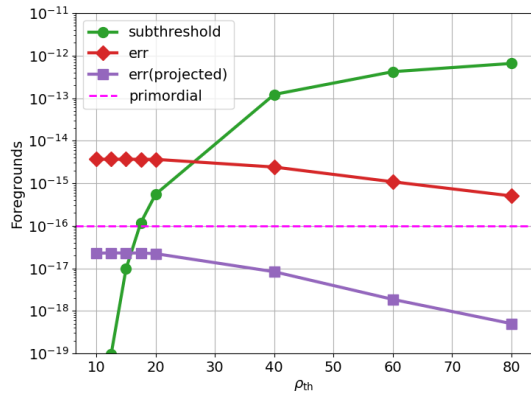


FIG. 6. Components of the BNS foreground at the frequency of 0.2 Hz where DECIGO is the most sensitive to SGWB. The red diamonds and purple squares are the error components without and with the projection scheme, respectively. The green circles are the subthreshold components. The magenta dashed line is the primordial SGWB. For $\rho_{\text{th}} = 10.0$, the subthreshold component returns 0.0 that means that there are no subthreshold events.

shows that the projection scheme will play a crucial role in detecting the primordial SGWB by DECIGO.

Figure 5 shows the foreground assessments for BBHs. We set $R(z = 0) = 20 \text{ Gpc}^{-3} \text{yr}^{-1}$ and $\rho_{\text{th}} = 10$. The amplitude of the total foreground, which is indicated by the black solid line, is one order of magnitude larger than that of BNSs. Each BBH signal of which the foreground consists tends to have a larger amplitude than a BNS. Therefore, DECIGO can detect more distant BBHs than BNSs; the subthreshold component will be reduced to a level that it does not affect the detection of the primordial SGWB. The subtraction error (indicated by the red line) in the BBH case is also smaller than that of the BNS case, though it is not small enough to detect SGWB. We conclude that the projection scheme is also crucial for removing the foreground of BBHs.

Figure 6 shows the components of the foregrounds

formed by BNS for various SNR thresholds. We fix the frequency at 0.2 Hz where DECIGO is the most sensitive to SGWB. As the threshold increases, the subthreshold components become larger while the subtraction error components with and without the projection slowly decrease. This figure indicates that, in order to subtract the signals from BNSs and lower the foreground level enough small to detect the primordial SGWB (2.13), we need to set the SNR threshold lower than ~ 15 and implement the projection scheme. For BBHs, we found that all events can be detected even with the threshold of 20, with no subthreshold components. However, we still need the projection scheme, as the subtraction errors without it are higher than the primordial SGWB.

IV. CONCLUSION AND DISCUSSION

The ultimate configuration of DECIGO would be able to detect the primordial SGWB. Although it has high sensitivity, a large number of compact binaries forming the foreground hinders the detection of the primordial SGWB. Detecting the compact binaries as individual events and subtracting them is a crucial strategy for detecting the primordial SGWB in DECIGO. In this paper, we assessed the amplitude of the foreground by using the population model inferred from the latest LVK observation. We found that the projection scheme allows us to remove both the foregrounds of BBH and BNS and suppress them enough to detect the primordial SGWB.

Regarding the feasibility of the subtraction, we compare the total number of source parameters and the number of data points available in the strain data. Assuming the local merger rate of $100 \text{ Gpc}^{-3} \text{yr}^{-1}$ and the population model of GWTC4, the total number of BNSs is about 8×10^5 . Each of them is characterized by ~ 10 source parameters. The total number of parameters to be estimated is about 8×10^6 . On the other hand, assuming the observational period of 3 yr and the sampling rate of 1 Hz, we estimate the total number of data points in the strain data to be about 2×10^8 , which is larger than the total number of parameters to be estimated. In this sense, it is feasible to estimate the best-fit parameters for all BNSs. Practically, the computational cost for the parameter estimation is a serious problem. Furthermore, in the deci Hz frequency band, the binary signals have long durations, which require a higher computational cost. Even in LVK analysis, the full-parameter estimation takes several hours for a BBH merger signal and several days for a BNS signal. There are several sophisticated techniques for efficiently estimating the source parameters (heterodyned likelihood [17, 18], relative binning [19, 20], singular value decomposition of a template bank [21], and simulation based inference [22–27]). Evaluating their sensitivity and required computational resources is important to demonstrate DECIGO is feasible for detecting the primordial SGWB.

We did not mention the foregrounds generated by

white dwarf binaries that will merge around $\mathcal{O}(10^{-2} \text{ Hz})$. They are also the source of the astrophysical foreground. For example, Staelens *et al.* [28] evaluated the foregrounds generated by the white dwarf binaries. It has a peak around 0.01 Hz and rapidly decreases as the frequency increases. Even if most of them remain as background after the subtraction, they will affect only below 0.1 Hz, which will not hurt the detectability of DECIGO for the primordial SGWB. We need to conduct further investigation to clarify the practical aspects of the foreground from white dwarf binaries.

ACKNOWLEDGMENTS

The authors are grateful to Nobuyuki Kanda and Takahiro Tanaka for fruitful discussions, and to Kazunori Kohri and Xingjiang Zhu for their insightful comments. This work is supported by JSPS KAKENHI Grant No. JP23K13099, JP23H04502.

We used the software: `numpy` [29], `scipy` [30], `matplotlib` [31], `astropy` [32–34].

Appendix A: Cutler and Harms' projection strategy

In this appendix, we explain how we assessed the subtraction errors in Eqs. (2.29) and (2.31).

1. Best-fit waveform

The log-likelihood that the strain data d contains the GW signal $h(\theta)$ is given by

$$\Lambda(d \mid \theta) = -\frac{1}{2} \langle d - h(\theta) \mid d - h(\theta) \rangle. \quad (\text{A1})$$

The bracket notation, $\langle a \mid b \rangle$, is the noise-weighted inner product defined by

$$\langle a \mid b \rangle = 4 \operatorname{Re} \int_0^\infty df \frac{\tilde{a}^*(f) \tilde{b}(f)}{S_n(f)}. \quad (\text{A2})$$

We assume that GW signal $\hat{h} := h(\hat{\theta})$ with the true parameter exists in the strain data d , written by

$$d = \hat{h} + n, \quad (\text{A3})$$

with the detector noise n . The best-fit parameter, θ_{bf} , is defined as the parameter θ where the log-likelihood becomes its maximum. From the definition of the log-likelihood (A1), we get

$$\langle \partial_i h_{\text{bf}} \mid \hat{h} - h_{\text{bf}} \rangle + \langle \partial_i h_{\text{bf}} \mid n \rangle = 0, \quad (\text{A4})$$

where ∂_i is the partial derivative with respect to i th parameter of θ . The bestfit waveform is denoted by

$h_{\text{bf}} := h(\theta_{\text{bf}})$. We denote the deviation of the best-fit parameter from the true value by $\Delta\theta$,

$$\Delta\theta = \theta_{\text{bf}} - \hat{\theta}. \quad (\text{A5})$$

We define the residual δh that will be left after subtracting the bestfit waveform h_{bf} from the true signal \hat{h} , that is

$$\delta h = \hat{h} - h_{\text{bf}}. \quad (\text{A6})$$

Assuming the deviation of the best-fit parameter from the true value is small enough, we perform the Taylor expansion of δh around $\Delta\theta = 0$ as

$$\begin{aligned} \delta h &= \hat{h} - \left\{ \hat{h} + \Delta\theta_i \partial_i h_{\text{bf}} + \frac{1}{2} \Delta\theta_i \Delta\theta_j \partial_i \partial_j h_{\text{bf}} + \dots \right\} \\ &= -\Delta\theta_i \partial_i h_{\text{bf}} - \frac{1}{2} \Delta\theta_i \Delta\theta_j \partial_i \partial_j h_{\text{bf}} + \dots \end{aligned} \quad (\text{A7})$$

Here, we use the Einstein summation convention. Substituting Eq. (A7) into Eq. (A4), we get

$$0 = -\langle \partial_i h_{\text{bf}} \mid \partial_j h_{\text{bf}} \rangle \Delta\theta_j + \langle \partial_i h_{\text{bf}} \mid n \rangle + O(\Delta\theta^2). \quad (\text{A8})$$

The deviation $\Delta\theta_i$ can be written by

$$\Delta\theta_i = (\Gamma_{\text{bf}}^{-1})_{ij} \langle \partial_j h_{\text{bf}} \mid n \rangle, \quad (\text{A9})$$

where Γ is the Fisher matrix,

$$\Gamma_{ij}(\theta) = \langle \partial_i h(\theta) \mid \partial_j h(\theta) \rangle, \quad (\text{A10})$$

and $(\Gamma_{\text{bf}})_{ij} = \Gamma_{ij}(\theta_{\text{bf}})$. The covariance of $\Delta\theta$ is obtained by

$$\overline{\Delta\theta_i \Delta\theta_j} = (\Gamma_{\text{bf}}^{-1})_{ij}. \quad (\text{A11})$$

We get a rough estimation of the power of the residual δh ,

$$\overline{\langle \delta h \mid \delta h \rangle} = \frac{\overline{\Delta\theta_i \Delta\theta_j} \langle \partial_i h_{\text{bf}} \mid \partial_j h_{\text{bf}} \rangle}{\langle h \mid h \rangle} = \frac{N_p}{\rho^2}. \quad (\text{A12})$$

up to the fourth order of $\Delta\theta$. Here, N_p is the number of source parameters. We use Eq. (A12) for assessing the residual components Ω_{err} in Eq. (2.29).

2. Projection

We define the projection operator P and the projected residual $\delta^P h$ by

$$\delta^P h = P[\delta h] = \delta h - (\partial_i h_{\text{bf}})(\Gamma_{\text{bf}}^{-1})_{ij} \langle \partial_j h_{\text{bf}} \mid \delta h \rangle. \quad (\text{A13})$$

Substituting the Taylor expansion of δh with respect to the $\Delta\theta$ and keeping up to the second order of $\Delta\theta$, we get

$$\begin{aligned} \delta^P h &= -\frac{1}{2} \Delta\theta_i \Delta\theta_j \partial_i \partial_j h_{\text{bf}} \\ &\quad + \Delta\theta_i \Delta\theta_j (\partial_k h_{\text{bf}})(\Gamma_{\text{bf}}^{-1})_{k\ell} \langle \partial_\ell h_{\text{bf}} \mid \partial_i \partial_j h_{\text{bf}} \rangle. \end{aligned} \quad (\text{A14})$$

We get the power of the projected residual as

$$\langle \delta^P h | \delta^P h \rangle = \frac{1}{4} \Delta\theta_i \Delta\theta_j \Delta\theta_k \Delta\theta_\ell \langle \partial_i \partial_j h_{\text{bf}} | \partial_k \partial_\ell h_{\text{bf}} \rangle \quad (\text{A15})$$

Evaluating this with the rough estimation where $\partial^2 h \sim (\partial h)^2/h \sim \Gamma/h$ and $(\Delta\theta)^2 \sim \Gamma^{-1}$, we get

$$\frac{\overline{\langle \delta^P h | \delta^P h \rangle}}{\langle h | h \rangle} \sim \frac{N_p^2}{\rho^4}. \quad (\text{A16})$$

We use this in Eq. (2.31).

[1] S. Kawamura et al., PTEP **2021**, 05A105 (2021), arXiv:2006.13545 [gr-qc].

[2] S. Biscoveanu, C. Talbot, E. Thrane, and R. Smith, Phys. Rev. Lett. **125**, 241101 (2020), arXiv:2009.04418 [astro-ph.HE].

[3] N. J. Cornish and J. Crowder, Phys. Rev. D **72**, 043005 (2005), arXiv:gr-qc/0506059.

[4] T. Littenberg, N. Cornish, K. Lackeos, and T. Robson, Phys. Rev. D **101**, 123021 (2020), arXiv:2004.08464 [gr-qc].

[5] M. Colpi et al. (LISA), LISA Definition Study Report (2024), arXiv:2402.07571 [astro-ph.CO].

[6] R. Rosati and T. B. Littenberg, Phys. Rev. D **112**, 084060 (2025), arXiv:2410.17180 [gr-qc].

[7] C. Cutler and J. Harms, Phys. Rev. D **73**, 042001 (2006), arXiv:gr-qc/0511092.

[8] X.-J. Zhu, E. J. Howell, D. G. Blair, and Z.-H. Zhu, Mon. Not. Roy. Astron. Soc. **431**, 882 (2013), arXiv:1209.0595 [gr-qc].

[9] P. A. Rosado, Phys. Rev. D **84**, 084004 (2011), arXiv:1106.5795 [gr-qc].

[10] N. Seto, S. Kawamura, and T. Nakamura, Phys. Rev. Lett. **87**, 221103 (2001), arXiv:astro-ph/0108011.

[11] K. Yagi and N. Seto, Phys. Rev. D **83**, 044011 (2011), [Erratum: Phys. Rev. D 95, 109901 (2017)], arXiv:1101.3940 [astro-ph.CO].

[12] N. Aghanim et al. (Planck), Astron. Astrophys. **641**, A6 (2020), [Erratum: Astron. Astrophys. 652, C4 (2021)], arXiv:1807.06209 [astro-ph.CO].

[13] A. G. Abac et al. (LIGO Scientific, VIRGO, KAGRA), Upper Limits on the Isotropic Gravitational-Wave Background from the first part of LIGO, Virgo, and KAGRA's fourth Observing Run (2025), arXiv:2508.20721 [gr-qc].

[14] A. G. Abac et al. (LIGO Scientific, VIRGO, KAGRA), GWTC-4.0: Updating the Gravitational-Wave Transient Catalog with Observations from the First Part of the Fourth LIGO-Virgo-KAGRA Observing Run (2025), arXiv:2508.18082 [gr-qc].

[15] A. G. Abac et al. (LIGO Scientific, VIRGO, KAGRA), GWTC-4.0: Population Properties of Merging Compact Binaries (2025), arXiv:2508.18083 [astro-ph.HE].

[16] 10.5281/zenodo.16911563 (2025).

[17] N. J. Cornish, Fast Fisher Matrices and Lazy Likelihoods (2010), arXiv:1007.4820 [gr-qc].

[18] N. J. Cornish, Phys. Rev. D **103**, 104057 (2021), arXiv:2101.01188 [gr-qc].

[19] B. Zackay, L. Dai, and T. Venumadhav, Relative Binning and Fast Likelihood Evaluation for Gravitational Wave Parameter Estimation (2018), arXiv:1806.08792 [astro-ph.IM].

[20] K. Krishna, A. Vijaykumar, A. Ganguly, C. Talbot, S. Biscoveanu, R. N. George, N. Williams, and A. Zimmerman, Accelerated parameter estimation in Bilby with relative binning (2023), arXiv:2312.06009 [gr-qc].

[21] K. Cannon, A. Chapman, C. Hanna, D. Keppel, A. C. Searle, and A. J. Weinstein, Phys. Rev. D **82**, 044025 (2010), arXiv:1005.0012 [gr-qc].

[22] K. Cranmer, J. Brehmer, and G. Louppe, Proc. Nat. Acad. Sci. **117**, 30055 (2020), arXiv:1911.01429 [stat.ML].

[23] S. R. Green, C. Simpson, and J. Gair, Phys. Rev. D **102**, 104057 (2020), arXiv:2002.07656 [astro-ph.IM].

[24] A. Delaunoy, A. Wehenkel, T. Hinderer, S. Nisanke, C. Weniger, A. R. Williamson, and G. Louppe, Lightning-Fast Gravitational Wave Parameter Inference through Neural Amortization (2020), arXiv:2010.12931 [astro-ph.IM].

[25] M. Dax, S. R. Green, J. Gair, M. Deistler, B. Schölkopf, and J. H. Macke, Group equivariant neural posterior estimation (2021), arXiv:2111.13139 [cs.LG].

[26] M. Dax, J. Wildberger, S. Buchholz, S. R. Green, J. H. Macke, and B. Schölkopf, Flow Matching for Scalable Simulation-Based Inference (2023), arXiv:2305.17161 [cs.LG].

[27] V. Raymond, S. Al-Shammari, and A. Göttel, Mon. Not. Roy. Astron. Soc. **1103**, 1108 (2025), arXiv:2406.03935 [gr-qc].

[28] S. Staelens and G. Nelemans, Astron. Astrophys. **683**, A139 (2024), arXiv:2310.19448 [astro-ph.HE].

[29] C. R. Harris et al., Nature **585**, 357 (2020), arXiv:2006.10256 [cs.MS].

[30] P. Virtanen et al., Nature Meth. **17**, 261 (2020), arXiv:1907.10121 [cs.MS].

[31] J. D. Hunter, Comput. Sci. Eng. **9**, 90 (2007).

[32] T. P. Robitaille et al. (Astropy), Astron. Astrophys. **558**, A33 (2013), arXiv:1307.6212 [astro-ph.IM].

[33] A. M. Price-Whelan et al. (Astropy), Astron. J. **156**, 123 (2018), arXiv:1801.02634.

[34] A. M. Price-Whelan et al. (Astropy), Astrophys. J. **935**, 167 (2022), arXiv:2206.14220 [astro-ph.IM].